

SRAW-Attack: Space-Reweighted Adversarial Warping Attack for SAR Target Recognition

Yiming Zhang, Weibo Qin, Yuntian Liu, *Student Member, IEEE*, and Feng Wang, *Member, IEEE*

Abstract—Synthetic aperture radar (SAR) imagery exhibits intrinsic information sparsity due to its unique electromagnetic scattering mechanism. Despite the widespread adoption of deep neural network (DNN)-based SAR automatic target recognition (SAR-ATR) systems, they remain vulnerable to adversarial examples and tend to over-rely on background regions, leading to degraded adversarial robustness. Existing adversarial attacks for SAR-ATR often require visually perceptible distortions to achieve effective performance, thereby necessitating an attack method that balances effectiveness and stealthiness. In this paper, a novel attack method termed Space-Reweighted Adversarial Warping (SRAW) is proposed, which generates adversarial examples through optimized spatial deformation with reweighted budgets across foreground and background regions. Extensive experiments demonstrate that SRAW significantly degrades the performance of state-of-the-art SAR-ATR models and consistently outperforms existing methods in terms of imperceptibility and adversarial transferability. Code is made available at <https://github.com/boremycin/SAR-ATR-TransAttack>.

Index Terms—Adversarial attack, automatic target recognition, image warping, transferability, synthetic aperture radar (SAR).

I. INTRODUCTION

Deep neural network (DNN)-based synthetic aperture radar (SAR) Automatic Target Recognition (SAR-ATR) has become the paradigm of high-resolution SAR image interpretation. However, it is inherently vulnerable to elaborately designed inputs termed adversarial examples, which can induce erroneous predictions [1]. Motivated by this vulnerability, numerous well-established [2-6] as well as recent state-of-the-art (SOTA) [7-9] adversarial attack approaches for optical images have emerged. In the SAR domain, related studies [10-12] have begun to incorporate SAR-specific characteristics, such as microwave-based imaging mechanisms and clutter-dominated grayscale representations [13], into adversarial attack strategies. Nevertheless, how to design attack mechanisms that are both effective and well-aligned with the unique properties of SAR imagery remains an open problem.

The computations in this research were performed using the CFFF platform of Fudan University. (*Corresponding author: Feng Wang*).

Yiming Zhang, Weibo Qin, Yuntian Liu, and Feng Wang are with the Key Laboratory for Information Science of Electromagnetic Waves, Ministry of Education, School of Information Science and Technology, Fudan University (FDU), Shanghai, 200433, China (e-mail: zhangyiming25, wbqin21@m.fudan.edu.cn, fengwang@fudan.edu.cn)

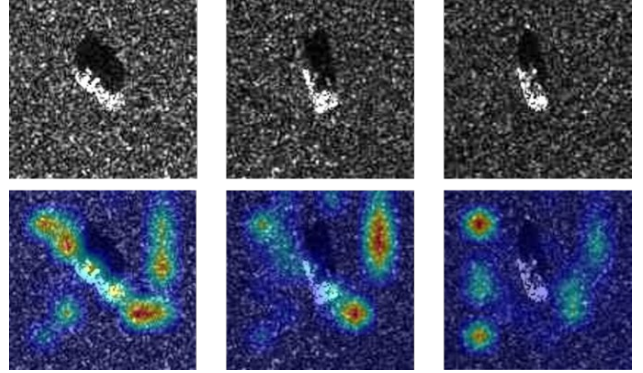


Fig. 1. Grad-CAM-based [14] attention heatmap visualization of SAR images, highlighting the discriminative regions exploited by the DNN for target recognition.

SAR imagery has been confirmed to exhibit pronounced background correlation [15-17], whereby clutter regions with limited semantic content exert a non-negligible influence on SAR-ATR predictions. Belloni et al. [18] further analyzed the interplay among different components, while Li et al. [19] pointed out that biases in SAR data introduce non-causal correlations, encouraging DNNs to overfit background clutter. When the DNNs over-parameterized for optical imagery are applied to SAR data, the relatively monotonic background can induce a form of negative robustness, leading models to over-rely on contextual cues rather than target-specific scattering features. As illustrated in Fig. 1, Grad-CAM [14] reveals that the model’s attention is more concentrated on background regions than on the target foreground.

In contrast to optical imagery, where adversarial examples are typically imperceptible [20], the intrinsic information sparsity of SAR data, caused by the electromagnetic scattering mechanism [15, 19], often necessitates more perceptible perturbations to achieve effective attacks, thereby severely undermining their stealthiness. Since the background perturbations are generally less perceptible, a natural strategy is to impose heterogeneous perturbation budgets between foreground and background, assigning aggressive alterations in the background while preserving target consistency. In addition, transformation-based attack methods [7, 8] have been proven to boost both attack effectiveness and transferability. Meanwhile, SAR imagery is sensitive to geometric structure, and subtle topological deformations can shift key scatter centers [12]. Based on the above analysis, introducing spline-based warping [21] spatial deformation mechanisms into adversarial generation exhibits significant potential for SAR-ATR, as it enables effective manipulation of background-dependent cues while maintaining a favorable

balance between attack effectiveness and perceptual imperceptibility.

In this letter, a novel adversarial method for SAR imagery is proposed, termed **Space-Reweighted Adversarial Warping (SRAW)**, which generates adversarial examples via spatial warping. Instead of directly optimizing input pixels through gradient ascent, SRAW incorporates the Thin-Plate Splines (TPS)—based spatial deformation [21] and reformulates adversarial generation as an optimization over warping control points. These control points are updated through gradient-based iterations under space-reweighted deformation constraints between foreground and background regions, enabling an effective and stealthy adversarial configuration.

In summary, the main contributions of this letter are as follows:

- 1) We identify a fundamental dilemma of adversarial attacks for SAR imagery, where the intrinsic information sparsity of SAR data causes effective attacks to rely on stronger and more perceptible perturbations, making it difficult to simultaneously achieve effectiveness and stealthiness.
- 2) A novel SAR-specific attack termed Space-Reweighted Adversarial Warping (SRAW) is proposed, which integrates spatial warping with a tailored foreground-background reweighting strategy. This work is among the first works to employ spatial warping as the primary mechanism for generating SAR adversarial examples.
- 3) Extensive experiments on the MSTAR dataset demonstrate that SRAW consistently outperforms existing established and SOTA attacks in terms of attack success while preserving remarkably improved imperceptibility.

II. METHODOLOGY

A. Preliminaries and Problem Formulation

The input benign image is denoted as $x \in \mathbb{R}^{w \times h}$ with its class label $y \in \{1, 2, \dots, m\}$. A DNN model $f(\cdot)$ serves as a SAR-ATR classifier, where $f(x; \theta) = y$, m denotes the number of classes, and θ represents the learned parameters of the target model. As for perturbation-adding attacks, the goal is to craft an adversarial example $x^{adv} = x + \delta$ with the elaborately designed perturbation δ to mislead the target model into making incorrect predictions, i.e., $f(x^{adv}; \theta) \neq y$. To guarantee that the adversarial example remains imperceptible, δ is limited to a bounded ℓ_p -norm with the perturbation budget ϵ . Following the widely used setting, the perturbation is constrained by the ℓ_∞ -norm in this paper. Accordingly, the generation of adversarial examples can be formulated as the following optimization problem:

$$\arg \max_{x^{adv}} \mathcal{L}(f(x^{adv}), y), \quad s.t. \quad \|\delta\|_\infty \leq \epsilon, \quad (1)$$

where \mathcal{L} is the cross-entropy loss, which is commonly applied to DNN models.

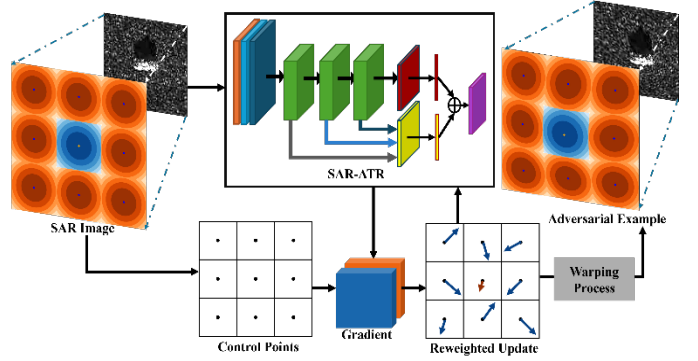


Fig. 2. Illustration of our SRAW method.

Nonetheless, for more general scenarios, it is arduous to directly manipulate the target model as in (1), and the more practical implementation is to iteratively produce adversarial examples via a surrogate model $f_{sur}(\cdot)$ and mislead the target model through the transferability of adversarial examples, referred to as the black-box attack setting. Hence, the $(t + 1)$ -th optimization iteration can be formulated as:

$$x_{t+1}^{adv} = Clip_\epsilon\{x_t^{adv} + \alpha \cdot sign(\nabla_{x_t^{adv}} \mathcal{L}(f_{sur}(x_t^{adv}, y)))\}, \quad (2)$$

where $Clip_\epsilon(\cdot)$ denotes the ℓ_∞ -norm constrain that restricts the perturbation within an ϵ -radius; α is the iterative step size; $sign(\cdot)$ denotes the sign function and $\nabla_{x_t^{adv}} \mathcal{L}(\cdot)$ represents the gradient of the loss with respect to the adversarial example at iteration t .

B. TPS-Based Spatial Deformation

Considering the trade-off between attack effectiveness and concealment, an initial motivation is to convert the generating paradigm by replacing additive perturbation with spatial deformation. According to the core of the TPS warping algorithm [21], the spatial deformation consists of two main steps: solving the warping parameters and performing the image interpolation. The first step requires two sets of control-point coordinates, i.e.,

$$\Gamma_{src} = \{(u_i, v_i)\}_{i=1}^N, \quad \Gamma_{tar} = \{(u'_i, v'_i)\}_{i=1}^N, \quad (3)$$

where Γ_{src} and Γ_{tar} denote the source and target control-point sets respectively, and (u_i, v_i) or (u'_i, v'_i) is the i -th point among the set of N control points.

To minimize the bending energy and ensure a smooth interpolation of the deformation effect, the TPS algorithm utilizes the radial basis function:

$$U(r) = r^2 \ln(r). \quad (4)$$

This kernel quantifies the geometric deformation between Γ_{src} and Γ_{tar} . Given that planar coordinate mapping can be decomposed into two separate scalar fields along the u -direction and v -direction, the spline functions that act as the interpolation mappings can be written as:

$$g_{u'}(u, v) = a_1 + a_u u + a_v v + \sum_{i=1}^N w_i U(\|\mathbf{P}_i - (u, v)\|), \quad (5)$$

$$g_{v'}(u, v) = b_1 + b_u u + b_v v + \sum_{i=1}^N w'_i U(\|\mathbf{P}_i - (u, v)\|), \quad (6)$$

where a_1, a_u, a_v and b_1, b_u, b_v are the affine coefficients, w_i and w'_i are the non-affine kernel weights associated with the i -th source control point $\mathbf{P}_i = (u_i, v_i)$. The coefficients can be solved through the following linear system:

$$\begin{bmatrix} \mathbf{K} & \boldsymbol{\Gamma}_{src} \\ \boldsymbol{\Gamma}_{src}^T & \mathbf{O} \end{bmatrix} \times \begin{bmatrix} \mathbf{w} \\ \mathbf{a} \end{bmatrix} = \begin{bmatrix} \boldsymbol{\Gamma}_{tar} \\ \mathbf{O} \end{bmatrix}, \quad (7)$$

where \mathbf{K} is the kernel matrix defined by $K_{ij} = U(\|\mathbf{P}_i - \mathbf{P}_j\|)$, \mathbf{w} and \mathbf{a} denote the non-affine and affine TPS coefficients, respectively.

Given the solved TPS parameters, image interpolation is performed by remapping input pixels according to (5) and (6), using bicubic interpolation. Consequently, the overall deformation applied to the input x to yield warped output x' can be formulated as the transformation function $\mathcal{T}(\cdot)$ defined as follows:

$$x' = \mathcal{T}(x, \boldsymbol{\Gamma}_{src}, \boldsymbol{\Gamma}_{tar}). \quad (8)$$

From the perspective of adversarial equivalence to perturbation-adding attacks, the warped image x' is directly optimized through the target loss. By applying the chain rule of differentiation, the gradient can be written as:

$$\nabla_{\Gamma} \mathcal{L} = \frac{\partial \mathcal{L}}{\partial x'} \cdot \frac{\partial \mathcal{T}(x, \boldsymbol{\Gamma})}{\partial \boldsymbol{\Gamma}}. \quad (9)$$

The spline-based formulation in (5)-(6) parameterizes spatial deformation on a low-dimensional smooth manifold, effectively constraining the search space and facilitating stable adversarial optimization.

C. Proposed SRAW Attack

To capitalize on the inherent negative robustness of DNN-based SAR-ATR and enhance the imperceptibility of the resulting adversarial examples, we propose a **Space-Reweighted Adversarial Warping (SRAW)** attack. The method integrates TPS-based spatial deformation into a momentum-based gradient-driven framework, thereby reformulating adversarial example generation as a spatial deformation optimization problem.

More precisely, the key factor governing the deformation behavior is the offsets $\boldsymbol{\xi}$ between $\boldsymbol{\Gamma}_{src}$ and $\boldsymbol{\Gamma}_{tar}$ when $\boldsymbol{\Gamma}_{src}$ is initially specified, which can thus be expressed as:

$$\boldsymbol{\xi} = \boldsymbol{\Gamma}_{tar} - \boldsymbol{\Gamma}_{src}. \quad (10)$$

In the SRAW attack, the source control-point set $\boldsymbol{\Gamma}_{src}$ is fixed by a priori spatial mesh partition, where the center of each grid cell is selected as a source control point. The total number of $\boldsymbol{\Gamma}_{src}$ is therefore determined by mesh width m_w and mesh height m_h . The optimization process can be restricted to the control-point offset $\boldsymbol{\xi}$. According to the formulations in (1) and (8), the adversarial example derived from the original input x is expressed as a spatially warped instance:

$$x^{adv} = \mathcal{T}(x, \boldsymbol{\xi}), \quad (11)$$

where $\mathcal{T}(\cdot)$ is parameterized by $\boldsymbol{\xi}$. Consequently, the adversarial-example generation can be cast as the following optimization problem:

$$\arg \max_{\boldsymbol{\xi}} \mathcal{L}(f(\mathcal{T}(x, \boldsymbol{\xi})), y). \quad (12)$$

Table I
CLASSIFICATION ACCURACY (%) OF TARGET MODELS

Model	Accuracy
DenseNet	99.65
VGG	98.16
ResNet	98.26
ResNext	96.22
PyramidNet	97.16

Due to the complex TPS mapping relationship and the dimensionality reduction to the control-point space, gradients obtained from a single backpropagation step may be noisy and deviate from the true descent direction. To obtain a more reliable update, a multiple-warping averaging strategy is adopted. Specifically, at the $(i+1)$ -th iteration, the aggregated gradient \bar{g}_{i+1} is computed as:

$$\bar{g}_{i+1} = \frac{1}{N_w} \sum_{j=1}^{N_w} g_j = \frac{1}{N_w} \sum_{j=1}^{N_w} \nabla_{\boldsymbol{\xi}} \mathcal{L}(f(\mathcal{T}(x_i^{adv}, \boldsymbol{\xi}_i)), y), \quad (13)$$

where N_w denotes the number of warped samples used for gradient averaging, and g_j is the gradient associated with the j -th warped sample.

To improve the stability and effectiveness of adversarial optimization, a momentum-based gradient update is adopted. At the $(i+1)$ -th iteration, the gradient g'_{i+1} is constructed by combining the current gradient g_{i+1} with the accumulated momentum g'_i . The momentum term suppresses gradient noise and promotes a consistent descent direction, resulting in smoother updates and faster convergence. The update rule is given by:

$$g'_{i+1} = \mu \cdot g'_i + \frac{\bar{g}_{i+1}}{\|\bar{g}_{i+1}\|}, \quad (14)$$

where μ represents the decay factor.

To preserve the visual plausibility of x^{adv} , the magnitude of spatial deformation is explicitly constrained. Based on the correspondence between mesh cells and foreground–background regions, the control-point offsets $\boldsymbol{\xi}$ can be naturally decomposed, i.e., $\boldsymbol{\xi} = \{\boldsymbol{\xi}_{fg}, \boldsymbol{\xi}_{bg}\}$. A tight displacement budget is imposed on $\boldsymbol{\xi}_{fg}$ to preserve target integrity, whereas a more permissive bound is applied to $\boldsymbol{\xi}_{bg}$, enabling stronger deformation to disrupt the reliance on contextual cues. The update of the control-point offsets at iteration $i+1$ follows a projected gradient step:

$$\boldsymbol{\xi}_{i+1} = \Pi_C(\boldsymbol{\xi}_i + \alpha \cdot g'_i), \quad (15)$$

where $\Pi_C(\cdot)$ is the projection onto the spatial-reweighted feasible set C determined by the region-dependent displacement limits r_{fg} and r_{bg} . Specifically,

$$C = \{\boldsymbol{\xi}: \|\boldsymbol{\xi}_{fg}\| \leq r_{fg}, \|\boldsymbol{\xi}_{bg}\| \leq r_{bg}\}, \quad (16)$$

and α is the step size.

II. EXPERIMENTS

A. Experimental Setup and Evaluation Measurement

In this paper, the widely used MSTAR [22] dataset published by the Defense Advanced Research Projects Agency

Table II
WHITE-BOX ASR (%) RESULTS OF TARGET MODELS

Method	DenseNet	VGG	ResNet	ResNext	PyramidNet	Average
FGSM	60.89	79.11	64.51	83.48	58.83	69.36
MI-FGSM	63.97	73.36	74.94	82.42	62.00	71.34
PGD	66.03	78.06	79.13	81.87	66.22	74.26
CW	62.43	75.45	68.69	85.08	60.42	70.41
LoRa-PGD	65.01	80.14	69.20	74.41	68.86	71.52
DeCoWa	67.58	76.49	76.51	80.81	65.16	73.31
SRAW	71.18	81.19	81.73	85.61	72.03	78.35

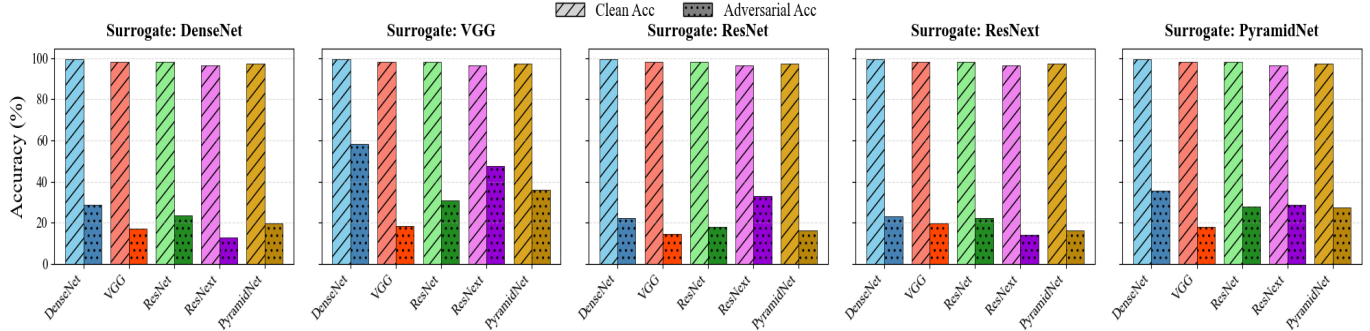


Fig. 3. Cross-model adversarial transferability of SRAW under black-box attacks. Each subfigure uses one surrogate model to generate adversarial examples, which are then evaluated on other target models. Lower prediction accuracy indicates stronger transferability.

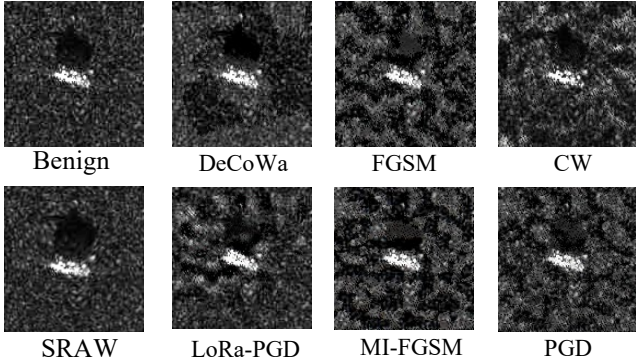


Fig.4 Visual comparison between the benign image and corresponding adversarial examples of all attack approaches.

Table III
PERCEPTUAL QUALITY EVALUATION ON VGG

Method	PSNR (dB) \uparrow	SSIM \uparrow	LPIPS \downarrow
FGSM	31.24	0.4567	0.3804
MI-FGSM	30.85	0.4369	0.4051
PGD	31.48	0.5109	0.3440
CW	29.01	0.5633	0.3521
LoRa-PGD	28.91	0.5251	0.4716
DeCoWa	26.86	0.4715	0.3829
SRAW	30.09	0.5724	0.2930

(DARPA) is adopted for our experiments. The dataset comprises SAR images across ten distinct vehicle categories

and is divided into training and test sets, with the test set additionally employed for adversarial attack evaluation.

To demonstrate the effectiveness and general applicability of the proposed SRAW attack, it is evaluated on a set of representative SOTA DNNs, including DenseNet [23], VGG [24], ResNet [25], ResNext [26], and PyramidNet [27]. The classification performance of these models is summarized in Table I, indicating that all selected targets achieve strong accuracy on the SAR-ATR task.

For a fair and comprehensive comparison, our method is evaluated against several widely used benchmark adversarial attacks, including FGSM [4], MI-FGSM [3], CW [6], and PGD [5], as well as SOTA approaches such as LoRa-PGD [9] and DeCoWa [7]. All methods are compared in terms of Attack Success Rate (ASR), which is defined using the indicator function $I(\cdot)$ as:

$$ASR = \frac{1}{N_c} \sum_{i=1}^{N_t} I(f(x_i) = y_i \wedge f(x_i^{adv}) \neq y_i), \quad (17)$$

where N_t represents the number of samples in the test set, and N_c is the number of benign samples that are correctly classified by the target model.

B. Attack Performance

White-box attack experiments are performed independently for each model and each method to compare their attack effectiveness. In this scenario, the target model is used to simultaneously generate and test the same adversarial examples. As reported in Table II, the proposed SRAW

outperforms all other approaches, achieving an average ASR of **78.35%** across all target models.

To further evaluate the adversarial transferability of SRAW under the black-box attack setting, each target model is alternatively treated as the surrogate model to generate adversarial examples, which are evaluated on the remaining target models. As illustrated in Fig. 3, SRAW induces a substantial degradation in prediction performance across diverse transfer scenarios. Specifically, when averaged over all surrogate models, the target models suffer an average accuracy drop by **73.33%**, manifesting the superior transferability and generalization capability of our method.

C. Evaluation of Attack Imperceptibility

The visualization of adversarial examples generated on VGG in Fig. 4 demonstrates that SRAW achieves significantly higher imperceptibility compared with competing approaches.

To precisely quantify the perceptual impact of image deformation, three widely used metrics are adopted: Peak Signal-to-Noise Ratio (PSNR), Structural Similarity Index (SSIM), and Learned Perceptual Image Patch Similarity (LPIPS) [28]. As reported in Table III for adversarial examples generated on VGG, SRAW achieves the **highest SSIM** and the **lowest LPIPS** among all compared methods, indicating superior structural preservation and perceptual invisibility. Although its PSNR is not the highest, the overall results demonstrate that SRAW provides a more favorable perceptual trade-off, yielding visually subtle yet effective adversarial examples.

IV. CONCLUSION

In this letter, we contend that the intrinsic information sparsity of SAR imagery induces a form of negative robustness in DNN-based SAR-ATR systems, leading to excessive reliance on background regions. Motivated by this insight, a novel attack method termed Space-Reweighted Adversarial Warping (SRAW) is proposed, which reformulates adversarial generation as the optimization of spatial warping with reweighted budgets on foreground and background regions.

Comprehensive experiments corroborate that SRAW consistently outperforms existing methods in terms of attack effectiveness and imperceptibility, while also exhibiting favorable transferability across models. Future work will explore the physical feasibility of SRAW by integrating it into the SAR signal formation and processing pipelines.

REFERENCES

- [1] C. Szegedy et al., "Intriguing properties of neural networks," *arXiv:1312.6199*, 2013.
- [2] A. Kurakin, I. J. Goodfellow, and S. Bengio, "Adversarial examples in the physical world," in *Artificial Intelligence Safety and Security*: Chapman and Hall/CRC, 2018, pp. 99–112.
- [3] Y. Dong et al., "Boosting adversarial attacks with momentum," in *Proc. IEEE Conf. Comput. Vis. Pattern Recognit. (CVPR)*, 2018, pp. 9185–9193.
- [4] I. J. Goodfellow, J. Shlens, and C. Szegedy, "Explaining and harnessing adversarial examples," *arXiv:1412.6572*, 2014.
- [5] A. Madry, A. Makelov, L. Schmidt, D. Tsipras, and A. Vladu, "Towards deep learning models resistant to adversarial attacks," *arXiv:1706.06083*, 2017.
- [6] N. Carlini and D. Wagner, "Towards evaluating the robustness of neural networks," in *Proc. IEEE Symp. Secur. Privacy (SP)*, 2017: IEEE, pp. 39–57.
- [7] Q. Lin et al., "Boosting adversarial transferability across model genus by deformation-constrained warping," in *Proc. AAAI Conf. Artif. Intell.*, 2024, vol. 38, no. 4, pp. 3459–3467.
- [8] K. Wang, X. He, W. Wang, and X. Wang, "Boosting adversarial transferability by block shuffle and rotation," in *Proc. IEEE Conf. Comput. Vis. Pattern Recognit. (CVPR)*, 2024, pp. 24336–24346.
- [9] D. Savostianova, E. Zangrando, and F. Tudisco, "Low-rank adversarial pgd attack," *arXiv:2410.12607*, 2024.
- [10] G. Zhang, S. Gao, X. Chang, and Y. Wang, "Physical-Domain SAR Universal Adversarial Perturbation Generation," *IEEE Trans. Aerosp. Electron. Syst.*, 2025.
- [11] I. Lemeire, Y. W. Law, S.-H. Lee, W. Meakin, and T.-J. Chin, "SAAIPAA: Optimizing aspect-angles-invariant physical adversarial attacks on SAR target recognition models," *arXiv:2511.03192*, 2025.
- [12] W. Qin, B. Long, and F. Wang, "Towards Model-Agnostic Adversarial Attack with Scattering Similarity for CNN-SAR Recognition," *IEEE Trans. Aerosp. Electron. Syst.*, 2025.
- [13] B. Peng, B. Peng, J. Zhou, J. Xia, and L. Liu, "Speckle-variant attack: Toward transferable adversarial attack to SAR target recognition," *IEEE Geosci. Remote Sens. Lett.*, vol. 19, pp. 1–5, 2022.
- [14] R. R. Selvaraju, M. Cogswell, A. Das, R. Vedantam, D. Parikh, and D. Batra, "Grad-cam: Visual explanations from deep networks via gradient-based localization," in *Proc. IEEE Int. Conf. Comput. Vis. (ICCV)*, 2017, pp. 618–626.
- [15] O. Kechagias-Stamatis and N. Aouf, "Automatic target recognition on synthetic aperture radar imagery: A survey," *IEEE Aerosp. Electron. Syst. Mag.*, vol. 36, no. 3, pp. 56–81, 2021.
- [16] C. Belloni, N. Aouf, J.-M. Le Caillec, and T. Merlet, "Comparison of descriptors for SAR ATR," in *Proc. IEEE Radar Conf. (RadarConf)*, 2019: IEEE, pp. 1–6.
- [17] M. Heiligers and A. Huizing, "On the importance of visual explanation and segmentation for SAR ATR using deep learning," in *Proc. IEEE Radar Conf. (RadarConf)*, 2018: IEEE, pp. 0394–0399.
- [18] C. Belloni, A. Balleri, N. Aouf, J.-M. Le Caillec, and T. Merlet, "Explainability of deep SAR ATR through feature analysis," *IEEE Trans. Aerosp. Electron. Syst.*, vol. 57, no. 1, pp. 659–673, 2020.
- [19] W. Li, W. Yang, L. Liu, W. Zhang, and Y. Liu, "Discovering and explaining the noncausality of deep learning in SAR ATR," *IEEE Geosci. Remote Sens. Lett.*, vol. 20, pp. 1–5, 2023.
- [20] Z. Guo et al., "Beyond vulnerabilities: A survey of adversarial attacks as both threats and defenses in computer vision systems," *arXiv:2508.01845*, 2025.
- [21] F. L. Bookstein, "Principal warps: Thin-plate splines and the decomposition of deformations," *IEEE Trans. Pattern Anal. Mach. Intell.*, vol. 11, no. 6, pp. 567–585, 2002.
- [22] E. R. Keydel, S. W. Lee, and J. T. Moore, "MSTAR extended operating conditions: A tutorial," in *Proc. SPIE Algorithms Synth. Aperture Radar Imagery III*, vol. 2757, pp. 228–242, 1996.
- [23] G. Huang, Z. Liu, L. Van Der Maaten, and K. Q. Weinberger, "Densely connected convolutional networks," in *Proc. IEEE Conf. Comput. Vis. Pattern Recognit. (CVPR)*, 2017, pp. 4700–4708.
- [24] K. Simonyan and A. Zisserman, "Very deep convolutional networks for large-scale image recognition," *arXiv:1409.1556*, 2014.
- [25] K. He, X. Zhang, S. Ren, and J. Sun, "Deep residual learning for image recognition," in *Proc. IEEE Conf. Comput. Vis. Pattern Recognit. (CVPR)*, 2016, pp. 770–778.
- [26] S. Xie, R. Girshick, P. Dollár, Z. Tu, and K. He, "Aggregated residual transformations for deep neural networks," in *Proc. IEEE Conf. Comput. Vis. Pattern Recognit. (CVPR)*, 2017, pp. 1492–1500.
- [27] D. Han, J. Kim, and J. Kim, "Deep pyramidal residual networks," in *Proc. IEEE Conf. Comput. Vis. Pattern Recognit. (CVPR)*, 2017, pp. 5927–5935.
- [28] R. Zhang, P. Isola, A. A. Efros, E. Shechtman, and O. Wang, "The unreasonable effectiveness of deep features as a perceptual metric," in *Proc. IEEE Conf. Comput. Vis. Pattern Recognit. (CVPR)*, 2018, pp. 586–595.